POD-based reduced order model for flows induced by rigid solids in forced rotation

Antoine Falaize, Erwan Liberge, Aziz Hamdouni

POD-based reduced order model for flows induced by rigid solids in forced rotation[☆]

Antoine Falaize[a,*], Erwan Liberge[a], Aziz Hamdouni[a]

[a] *LaSIE UMR 7356 CNRS ULR*
Université de La Rochelle
Avenue M. Crépeau
17042 La Rochelle, France

Abstract

This paper deals with the construction of reduced order models (ROMs) for the simulation of the interaction between a fluid and a rigid solid with imposed rotation velocity. The approach is a follows. First, we derive a monolithic description of the fluid/structure interaction by extending the Navier-Stokes equations from the fluid domain to the solid (rotor) domain similarly to the fictitious-domain approach. Second, we build a ROM by a proper orthogonal decomposition (POD) of the resulting multi-phases flow. This method consists in (i) constructing an optimal albeit empirical spatial basis for a very small subspace of the solution space, and (ii) projecting the governing equations on this reduced basis. Third, we cope with the reconstruction of the high-dimensional velocity field needed to evaluate the imposed velocity constraint by a POD of the solid membership function. Fourth, we use state of the art method to interpolate between available POD bases to build the proposed POD-ROM for a range of parameters values. The proposed method is applied to an academic configuration and proves efficient in the reconstruction of the velocity in both the fluid and solid domains while substantially reducing the computational cost.

Keywords: POD, ROM, Turbomachinery, FSI, Interpolation

[☆]This work is supported by the project ANR-15-CE08-0036, entitled *From HEating to COoling* (HECO), financed by the French National Research Agency (ANR). Further information is available at `http://www.agence-nationale-recherche.fr/Projet-ANR-15-CE08-0036`.

[*]Corresponding author
Email address: `antoine.falaize@univ-lr.fr` (Antoine Falaize)

Introduction

This work is concerned with the construction of reduced order models (ROMs) to speed-up the resolution of computational fluid dynamic (CFD) problems associated with flows induced by rigid solids with imposed rotation velocity. Such physical problems are involved in several applications of industrial interest (predictive simulation, active control, parametric shape optimization) in which axial fans or agitators play a major role (*e.g* turbomachinery, industrial furnaces and process engineering).

Flows induced by rotating solids are a special case of fluid/structure interaction (FSI), for which numerous computational methods are available (see *e.g.* [1] for FSI in general and [2, 3] for CFD methods dedicated to turbomachinery). Despite some limitations in the extensive use of CFD simulations when compared to experimental data [4, 5], this is the nowadays standard approach to the industrial design and performance analysis. Most of these methods can be divided in two categories [6]: *multi-domains* approaches and *multi-phases* approaches. In multi-domains approaches, the computational domain is divided into material subdomains over each a local model is solved [7, 8]. The global solution is then constructed by properly aggregating the local solutions. In mutli-phases approaches, a single equation with spatially dependent material properties is solved over the global computational domain. This includes *e.g.* the ficitious domains method [9, 10, 11, 12] (also called immersed volume method in [13, 14]), the immersed boundary method [15, 16], the ghost fluid method [15]. Both approaches yield computationally very expensive simulation codes despite efforts in the CFD community to reduce the complexity of the problem with simplifying assumptions, *e.g.* small disturbance assumption or boundary-layer assumption [17]. In particular, very fine meshing of the computational domain is usually needed to achieve high-fidelity simulation [18] leading to High-Dimensional Models (HDM) and thus, reliable reduced order

models (ROMs) are needed for design, parametric analysis and control.

The ROMs proposed in this paper are based on the well established Proper Orthogonal Decomposition (POD, also known as Karhunen-Loeve decomposition, SVD or PCA), introduced as a tools for the identification of coherent structures in dynamical systems in [19] based on previous works grounded in statistical analysis [20, 21, 22, 23]. This method proves efficient in the extraction of Proper Orthogonal Modes (POMs) associated with the evolution of complex large-scale dynamical systems (*e.g.* structural and fluid mechanics and electromagnetic) from experimental measurements or high-fidelity simulations. These POMs form a spatial basis onto which the governing equations are projected to build the so called POD-ROMs. Several previous works have been devoted to the construction of POD-ROMs for turbomachinery. In most approaches, the linearized Euler equations or linearized Navier-Stokes equations are considered, and the POD is performed in the frequency domain. This approach is justified by the usual geometric periodicity of the rotors in turbomachinery in general and axial fans or agitators in particular. It has been first proposed in [24, 25], and subsequently considered in [26, 17, 27]. More recently, the use of a weighted POD have been proposed in [28] to construct from experimental data a ROM for the axial-circumferential velocity profile associated with the steady axisymmetric parallel flow of an inviscid and incompressible fluid in a Francis turbine. Also, an Arnoldi procedure associated with a matching of transfer functions between original and reduced order model is proposed as a compromise to POD in [29]. These approaches suffer from two drawbacks. First, they yield accurate POD-ROMs only if the small disturbance assumption is verified so that the frequency domain analysis is justified. Second, they are not generally applicable and usually need dedicated CFD solvers.

In this work, we consider the non-linearized Navier-Stokes equations for flows in an incompressible newtonian fluid, and the POD is performed directly in the time domain over the d-dimensional velocity profile ($d = 2$ or 3). In order to

circumvent the incompatibility of the POD (which yields *spatial* modes) with moving domains (the rotating solids), we use a multi-phase approach. More precisely, the Navier-Stokes equations are extended to the solid domain in which the ensemble rotation velocity is enforced by a constraint relaxed through the definition of an appropriate distributed Lagrange multiplier. Note that the combination of the multi-phases approach and POD has been previously considered *e.g.* in [30, 31] for fluid structure interaction, in [32] for shape optimization and in [33] for feedback stabilization in FSI. However, the evaluation of the rigidity/velocity constraint in the solid usually requires the reconstruction of the full order solution at runtime, so that the simulation of the resulting POD-ROMs still depends on the number of degrees of freedom. In order to cope with the reconstruction of the full order velocity inside the solid domain, we propose in this work to benefit from the periodicity in the geometry of the rotors by applying the POD also to the characteristic function of the solid domain. The resulting POD-ROMs is independent of the number of degrees of freedom of the HDM, while preserving the accuracy of the standard approach. Additionally, any CFD software can be used to produce the snapshots from which the proper orthogonal basis is built (*non-intrusive* method).

However, it is known that ROMs built from POD are valid in the vicinity of the parameter used to produce the set of snapshots, *i.e.* they lack robustness with respect to changes in the parameters (see *e.g.* [27] for a parametric analysis in the context of turbomachinery and [34] for a mathematical *a priori* estimates of parametric sensibility in the context of CFD). That is, the simulation of the HDM must be performed for each new parameter to build the associated POMs so that the order reduction significance is lost. To circumvent the parametric robustness problem, some modified POD methods were proposed, such as global POD method, local POD method, and adaptive POD method (see *e.g.* [35] and references therein). In this work, we use a state of the art adaptive method to allow fast construction of the proposed POD-ROMs for a given parameter value by interpolating a set of precomputed POMs. The historically first adaptive

method have been proposed in [36, 37] and consists in the interpolation of the POMs over the tangent plane at a reference point on the Grassmann manifold. This method requires to properly select the reference point to achieve a good accuracy. Thus, we propose the use of the method introduced in [38] that consists in the extension of the Inverse Distance Weighting (IDW) interpolation method from vectorial spaces to Grassman manifolds which automatically adapts to the available sample of POMs.

This paper is organized as follows. The objectives and approach are detailed in the problem statement of section 1. The multi-phases governing equations for the coupled fluid/solid system used to construct the POD-ROMs are recalled in section 2. The two proposed POD-based low order dynamical systems are given in section 3. The parametric interpolation method is given in section 4. Finally, numerical results for an academic configuration are presented in section 5 before conclusions.

1. Problem statement

In this section, we shall define the domains configuration and the notations used in the remaining of the paper. Then, we state the data that are supposed to be available for the construction of the POD-ROMs. Finally, we detail the issues addressed in this work.

1.1. Domains definitions and notations

We consider the computational domain $\Omega \subset \mathbb{R}^d$ where d is the spatial dimension (usually 2 or 3) and the temporal domain $\mathrm{T} = [0, T] \subset \mathbb{R}^+$. The computational domain is filled with (i) a rotating solid $\mathtt{S}$ that occupies the physical domain $\Omega_{\mathtt{S}}(t)$ at time $t \in \mathrm{T}$ and (ii) an incompressible newtonian fluid $\mathtt{F}$, that is $\Omega = \Omega_{\mathtt{S}}(t) \cup \Omega_{\mathtt{F}}(t)$ (see figure 1). The domain boundary is denoted by $\Gamma = \partial\Omega$, the solid boundary is $\Gamma_{\mathtt{S}}(t) = \partial\Omega_{\mathtt{S}}(t)$ and the fluid boundary is $\Gamma_{\mathtt{F}}(t) = \Gamma \cup \Gamma_{\mathtt{S}}(t)$.

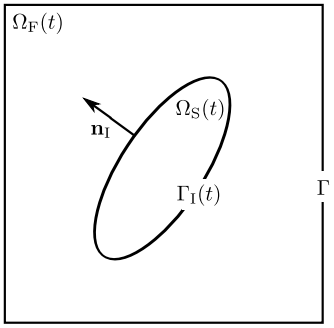

Figure 1: Schematic view of the computational domain $\Omega = \Omega_{\mathtt{S}}(t) \cup \Omega_{\mathtt{F}}(t)$.

The characteristic function of the solid domain is

$$\chi_{\mathtt{S}}(\boldsymbol{x}, t) = \begin{cases} 1 & \text{if } \boldsymbol{x} \in \Omega_{\mathtt{S}}(t), \\ 0 & \text{otherwise.} \end{cases} \tag{1}$$

In the case of turbomachinery, the solid (fan, agitator) is assumed to rotate around a given axis $\boldsymbol{e}_\omega$ passing through the center of rotation $\boldsymbol{x}_\omega$, at the angular velocity $\frac{\mathrm{d}\theta}{\mathrm{d}t}$, where θ is the angle with respect to a given reference position. The associated rotation velocity is

$$\boldsymbol{u}_{\boldsymbol{\omega}}(\boldsymbol{x}, t) = \boldsymbol{\omega} \times (\boldsymbol{x} - \boldsymbol{x}_\omega) \tag{2}$$

with $\boldsymbol{\omega} = \frac{\mathrm{d}\theta}{\mathrm{d}t}\, \boldsymbol{e}_\omega$ the rotation vector. The characteristic function is obtained at every time as the rotation of the initial configuration:

$$\chi_{\mathtt{S}}(\boldsymbol{x}, t) = R\big(\theta(t)\big)\, \chi_{\mathtt{S}}(\boldsymbol{x}, 0), \tag{3}$$

with $R(\theta)$ the rotation by angle θ about the axis $\boldsymbol{e}_\omega$.

1.2. Database construction

The first step toward the construction of POD-ROMs is the computation of the discrete approximation of the material velocity $\boldsymbol{u}_h : \Omega \times \mathrm{T} \times \mathbb{R}^p \to \mathbb{R}^d$ for a given parameter $\boldsymbol{p} \in \mathbb{R}^p$ on a reference (fixed) grid. Any CFD method can be used to simulate the HDM associated with the FSI problem described in the previous subsection, interpolating the results on the reference mesh if needed

(*e.g.* in case of moving meshes or remeshing solvers). we assume that sets of snapshots $\big(\mathbf{U}(\boldsymbol{p}_n)\big)_{1\leq n\leq n_p}$ have been generated for a variety of n_p parameters, where $\mathbf{U}$ denotes a set of n_T snapshots of the velocity stored as $U_{ij} = \boldsymbol{u}_h(\boldsymbol{x}_i, t_j)$ with $\boldsymbol{x}_i \in \Omega$ and $t_j \in \mathrm{T}$ for $i \in [1, \cdots, n_{\boldsymbol{x}}]$ and $j \in [1, \cdots, n_T]$.

1.3. Objectives and approach

The first objective of this work is to construct a POD-ROM that is able to reproduce the solution $\boldsymbol{u}_h(\boldsymbol{p})$ for a given parameter $\boldsymbol{p}$ over the time period T and beyond. The second objective is to construct the POD-ROM associated with a new parameter $\boldsymbol{p}^\star \notin (\boldsymbol{p}_n)_{1\leq n\leq n_p}$ from the snapshots obtained for the sets of snapshots $\big(\mathbf{U}(\boldsymbol{p}_n)\big)_{1\leq n\leq n_p}$.

The approach is as follows. First, we construct a low dimensional projection basis by POD of the snapshots associated with a given parameter (POMs). Second, reduced order models are constructed by projecting the problem equations onto a small subset of these POMs. Third, we interpolate between the POMs associated with the sets of snapshots $\big(\mathbf{U}(\boldsymbol{p}_n)\big)_{1\leq n\leq n_p}$ via robusts subspaces interpolation method to construct the POD-ROM associated with a new parameter $\boldsymbol{p}^\star \notin (\boldsymbol{p}_n)_{1\leq n\leq n_p}$.

2. Interaction between a fluid and a solid with imposed rotation velocity

In this section we adapt the *fictitious-domains method* introduced in [9, 10] and developed in [11] to the case of a flow induced by a solid with *imposed rotation velocity*. First, we detail the strong form of the governing equations. Second, we give the associated weak form. Third, we give the standard iterative method to solve the resulting saddle point problem which is the starting point in the derivation of the POD-ROMs in the next section 3.

2.1. Governing equations

The fluid domain $\Omega_{\mathtt{F}}$ is governed by the incompressible Navier-Stokes equations. To derive the governing equations for the solid domain and the fluid/structure interaction, we adopt an approach similar to the fictitious domain approach [10, 11] in which a monolithic formulation is derived by modeling the solid domain as a fluid with additional constraints to enforce rigidity. The difference here is that we enforce directly the ensemble rotation velocity to describe the motion of the rotor. The rotation constraint is given by

$$\boldsymbol{u}(\boldsymbol{x},t) - \boldsymbol{u}_{\boldsymbol{\omega}}(\boldsymbol{x},t) = \boldsymbol{0}, \quad \forall \boldsymbol{x} \in \Omega_{\mathtt{S}}(t) \ \text{ and } \ \forall t \in \mathrm{T}, \tag{4}$$

where $\boldsymbol{u} \in (\mathrm{H}^1(\Omega,\mathrm{T}))^d$ is the eulerian velocity with H^1 the standard Sobolev space. A direct consequence of (4) is that no deformation of the solid domain occurs:

$$\mathrm{D}\left(\boldsymbol{u}_{\mathtt{S}}\right) = \nabla \cdot \boldsymbol{u}_{\mathtt{S}} = 0, \quad \forall \boldsymbol{x} \in \Omega_{\mathtt{S}}(t), \ \forall t \in \mathrm{T}. \tag{5}$$

Thus, the incompressible Navier-Stokes equations can be extended to the solid domain provided an appropriate force term $\boldsymbol{\lambda} \in \left(\mathrm{L}^2(\Omega,\mathrm{T})\right)^d$ which ensures that the additional constraint (4) is verified. The strong form of the governing equations are then: find $\boldsymbol{u} \in \left(\mathrm{H}^1(\Omega,\mathrm{T})\right)^d$ such that $\forall \boldsymbol{x} \in \Omega$ and $\forall t \in \mathrm{T}$:

$$\left\{ \begin{array}{rcl} \rho \left(\dfrac{\partial \boldsymbol{u}}{\partial t} + \nabla \boldsymbol{u} \cdot \boldsymbol{u} \right) & = & \nabla \cdot \boldsymbol{\sigma} + \boldsymbol{f} - \boldsymbol{\lambda}, \\ \nabla \cdot \boldsymbol{u} & = & 0, \\ \chi_{\mathtt{S}}(\boldsymbol{u} - \boldsymbol{u}_{\boldsymbol{\omega}}) & = & 0, \end{array} \right. \tag{6}$$

where $\boldsymbol{\sigma} = 2\,\eta\,\mathrm{D}\left(\boldsymbol{u}\right) - p\,\boldsymbol{I}$ is the stress tensor with $\mathrm{D}\left(\boldsymbol{u}\right) = \frac{1}{2}\left(\nabla \boldsymbol{u} + {}^{\intercal}\nabla \boldsymbol{u}\right)$ the deformation rate tensor and $\boldsymbol{I}$ the d-dimensional identity tensor, ρ and η are respectively the fluid density and dynamic viscosity, and $\boldsymbol{f}$ are the volume forces acting on the material domain. Note that the pressure p can be interpreted as the Lagrange multiplier associated with the incompressibility constraint in (6). The problem (6) is equipped with the following set of boundary and initial

conditions:

$$\begin{cases} \boldsymbol{u}_{\mathtt{F}} = \boldsymbol{u}_{\mathtt{D}} & \forall \boldsymbol{x} \in \Gamma_{\mathtt{D}}, \quad \forall t \in \mathrm{T}, \\ \boldsymbol{\sigma}_{\mathtt{F}} \cdot \boldsymbol{n} = 0 & \forall \boldsymbol{x} \in \Gamma_{\mathtt{N}}, \quad \forall t \in \mathrm{T}, \\ \boldsymbol{u}(\boldsymbol{x},\, 0) = \boldsymbol{u}_0(\boldsymbol{x}) & \forall \boldsymbol{x} \in \Omega_{\mathtt{F}}(0), \quad t = 0, \end{cases} \tag{7}$$

with constant Dirichlet boundary condition on the boundary $\Gamma_{\mathtt{D}} \subseteq \Gamma$ and standard *outflow* boundary condition (zero normal stress) on the remaining boundary $\Gamma_{\mathtt{N}} = \Gamma \setminus \Gamma_{\mathtt{D}}$. The initial velocity $\boldsymbol{u}_0$ is assumed to be compatible with the constraint (4).

Remark 1 (Fluid/structure interaction)**.** *The interaction stress between the fluid and the solid on the interface* $\Gamma_{\mathtt{S}}$ *is naturally included in the proposed formulation. This can be shown by deriving (6) as in the fictitious domain method by an eulerian description of the standard local equilibrium equations for the solid and replacing the rigidity constraint* $\mathrm{D}(\boldsymbol{u}) = 0$ *by the imposed rotation in* $\Omega_{\mathtt{S}}$ *so that the boundary traction on* $\Gamma_{\mathtt{S}}$ *in each domain cancels.*

Remark 2 (Material properties)**.** *The density of the solid equals that of the fluid in the proposed formulation. This is justified by the fact that the velocity of the solid is imposed and is not impacted by the dynamics of the fluid nor by the action of the volume forces* $\boldsymbol{f}$*. Also, the* viscosity *of the solid equals that of the fluid. This is justified by the fact that this parameter has no physical meaning and must be considered as a scaling coefficient (see [14]).*

2.2. Weak formulation

Here, we precise the functional setting used to derive a standard weak formulation of (6) in view of the subsequent construction of the low order dynamical system. The velocity trial and test spaces are respectively

$$\mathrm{W} = \left\{ \boldsymbol{u} \in \left(\mathrm{H}^1(\Omega, \mathrm{T})\right)^d ;\ \boldsymbol{u} = \boldsymbol{u}_{\mathtt{D}}\ \forall \boldsymbol{x} \in \Gamma_{\mathtt{D}} \right\}, \quad \text{and} \tag{8}$$

$$\mathrm{W}_0 = \left\{ \boldsymbol{u} \in \left(\mathrm{H}^1(\Omega, \mathrm{T})\right)^d ;\ \boldsymbol{u} = \boldsymbol{0}\ \forall \boldsymbol{x} \in \Gamma_{\mathtt{D}} \right\}. \tag{9}$$

The pressure trial and test spaces are respectively

$$\mathrm{P}_0 = \left\{ p \in \mathrm{L}^2\big(\Omega, \mathrm{T}\big);\ \int_\Omega p(\boldsymbol{x}, t)\, \mathrm{d}\boldsymbol{x} = 0 \right\}, \quad \text{and} \quad \mathrm{L}^2\big(\Omega, \mathrm{T}\big). \tag{10}$$

Assuming that the solid domain never intersect with the computational boundary, the Lagrange multiplier trial and test spaces can be both chosen as W_0. The resulting week form of (6) is given by: find $\boldsymbol{u} \in \mathrm{W}$, $p \in \mathrm{P}_0$, $\boldsymbol{\lambda} \in \mathrm{W}_0$ such that

$$\rho \left(\frac{\partial \boldsymbol{u}}{\partial t} + \nabla \boldsymbol{u} \cdot \boldsymbol{u} \middle| \boldsymbol{v} \right) = (\boldsymbol{f} - \chi_{\mathrm{S}} \boldsymbol{\lambda} | \boldsymbol{v}) + (p | \nabla \cdot \boldsymbol{v}) - 2\,\eta\,(\mathrm{D}(\boldsymbol{u}) | \mathrm{D}(\boldsymbol{v})) \quad (11)$$

$$(\nabla \cdot \boldsymbol{u} | q) = 0, \quad (12)$$

$$(\chi_{\mathrm{S}} (\boldsymbol{u} - \boldsymbol{u}_{\boldsymbol{\omega}}) | \boldsymbol{\mu}) = 0, \quad (13)$$

for all $\boldsymbol{v} \in \mathrm{W}_0$, $q \in \mathrm{L}^2\big(\Omega, \mathrm{T}\big)$ and $\boldsymbol{\mu} \in \mathrm{W}_0$, with $(\bullet | \bullet)$ the inner product on $L^2(\Omega)$.

2.3. Iterative method

The weak form of the velocity constraint (13) can be relaxed iteratively using an augmented Lagrangian formulation coupled with an Uzawa algorithm (see [39] for details on this algorithm and [30, 14] for its application in FSI). The resulting iterative procedure to perform within each time step is described in algorithm 1. It is the the starting point in the derivation of the POD-ROMs of the next section 3.

3. Proposed reduced order models

In this section, we introduce the proposed low-order dynamical system associated with the governing equations (11–13). First, the momentum equation is projected on the POD basis associated with the velocity field. This yields a reduced order model which involves the reconstruction of the complete velocity field at each inner Uzawa iteration to evaluate the increment in the Lagrange multiplier. Thus, we propose a second reduced order model by (i) decomposing also the characteristic function onto a POD basis and (ii) building an explicit evaluation of the associated coefficients from the known solid angle. In this work, we use the classical *snapshot POD* method introduced in [40] and recalled in appendix Appendix A.

Data: Initial values $\boldsymbol{u}^0$, p^0 (*e.g.* from the previous time-step).

Result: $\boldsymbol{u}^\ell$ p^ℓ, $\boldsymbol{\lambda}^\ell$ solution of (11–13).

Initialize $\ell \leftarrow 0$, $\boldsymbol{\lambda}^\ell \leftarrow \mathbf{0}$, $e^\ell \leftarrow \infty$ and $\delta e^\ell \leftarrow \infty$;

while $e^\ell > \epsilon_{\text{tol}}$ *and* $\delta e^\ell > \epsilon_{\text{tol}}$ **do**

  Update $\ell \leftarrow \ell + 1$;

  Solve for $\boldsymbol{u}^\ell$, p^ℓ:

  $\rho \left(\delta_t \boldsymbol{u}^\ell + \nabla \boldsymbol{u}^\ell \cdot \boldsymbol{u}^\ell \middle| \boldsymbol{v}\right) - \left(\boldsymbol{f} - \chi_{\text{S}} \boldsymbol{\lambda}^{\ell-1} \middle| \boldsymbol{v}\right) - \left(p^\ell \middle| \nabla \cdot \boldsymbol{v}\right) +$
  $2\,\eta \left(\mathrm{D}\left(\boldsymbol{u}^\ell\right) \middle| \mathrm{D}\left(\boldsymbol{v}\right)\right) = 0,$

  $\left(\nabla \cdot \boldsymbol{u}^\ell \middle| q\right) = 0;$

  Update $\boldsymbol{\lambda}^\ell$:

  $\boldsymbol{\lambda}^\ell \leftarrow \boldsymbol{\lambda}^{\ell-1} + r\,\chi_{\text{S}} \left(\boldsymbol{u}^\ell - \boldsymbol{u}_{\boldsymbol{\omega}}\right)$;

  Check for convergence:

  $e^\ell \leftarrow \frac{\|\chi_{\text{S}}\,(\boldsymbol{u}^\ell - \boldsymbol{u}_{\boldsymbol{\omega}})\|_{\mathrm{L}^2(\Omega)}}{\|\chi_{\text{S}}\,\boldsymbol{u}_{\boldsymbol{\omega}}\|_{L^2(\Omega)}}$ and $\delta e^\ell \leftarrow e^{\ell-1} - e^\ell$;

end

Algorithm 1: Uzawa algorithm associated with the weak form of the governing equations (11–13).

3.1. Galerkin projection of the momentum equation

We suppose (discrete) solutions $(\boldsymbol{u}_h(\boldsymbol{x}, t_n))_{1 \le n \le n_T}$ of the governing equations (11–13) have been obtained. Each *snapshot* $\boldsymbol{u}_h(\boldsymbol{x}, t_n)$ is decomposed into a mean part $\overline{\boldsymbol{u}}_h(\boldsymbol{x})$ and a fluctuating part $\widetilde{\boldsymbol{u}}_h(\boldsymbol{x}, t)$, and the fluctuating part is decomposed over a POD basis $\boldsymbol{\Phi}^{\boldsymbol{u}} = (\boldsymbol{\phi}_i^{\boldsymbol{u}})_{1 \le i \le n_T}$ truncated to $n_{\boldsymbol{u}}$ modes:

$$\widehat{\boldsymbol{u}}_h(\boldsymbol{x}, t_n) = \overline{\boldsymbol{u}}_h(\boldsymbol{x}) + \sum_{i=1}^{n_{\boldsymbol{u}}} \boldsymbol{\phi}_i^{\boldsymbol{u}}(\boldsymbol{x})\, a_i(t_n), \tag{14}$$

where the set $\boldsymbol{a} = (a_i)_{1 \le i \le n_{\boldsymbol{u}}}$ collects the temporal coefficients of the fluctuating part of the velocity in the POD basis $\boldsymbol{\Phi}^{\boldsymbol{u}}$, which element are called velocity POD modes.

Remark 3 (Continuity equation)**.** *The mean field $\overline{\boldsymbol{u}}_h$ and the elements of $\boldsymbol{\Phi}^{\boldsymbol{u}}$ are built from linear combinations of the snapshots for $\boldsymbol{u}_h$ (see A.9), so that (i) the velocity POD modes are divergence free $\nabla \cdot \boldsymbol{\phi}_i^{\boldsymbol{u}} = 0$, $1 \le i \le n_{\boldsymbol{u}}$ and (ii) the*

approximation $\widehat{\boldsymbol{u}}_h$ automatically satisfies the continuity equation $\nabla \cdot \widehat{\boldsymbol{u}}_h = 0$.

Remark 4 (Dirichlet boundary conditions)**.** *The Dirichlet boundary conditions are supposed constant over time so that they are all included in the mean field $\overline{\boldsymbol{u}}(\boldsymbol{x})$, $\boldsymbol{x} \in \Gamma_{\mathtt{D}}$ and the velocity POD modes vanish on the boundary $\Gamma_{\mathtt{D}}$.*

Now performing a standard Galerkin projection of the governing equation (that is, using the ersatz (14) in place of $\boldsymbol{u}$ and the POMs $(\boldsymbol{\phi}_i^{\boldsymbol{u}}(\boldsymbol{x}))_{1\leq i\leq n_{\boldsymbol{u}}}$ in replacement of the test functions $\boldsymbol{v}$ in (11–13)) yields the following low-order dynamical system, referred as ROM1:

$$\mathbf{A} \cdot \frac{\mathrm{d}\boldsymbol{a}}{\mathrm{d}t} + \mathbf{B} \cdot \boldsymbol{a} + \mathbf{C} : \boldsymbol{a} \otimes \boldsymbol{a} + \mathbf{E}^{\ell} + \mathbf{F} = \mathbf{0}. \tag{15}$$

with the Uzawa update of the Lagrange multiplier

$$\boldsymbol{\lambda}^{\ell+1} = \boldsymbol{\lambda}^{\ell} + r\,\chi_{\mathtt{S}} \left(\overline{\boldsymbol{u}} + \sum_{i=1}^{n_{\boldsymbol{u}}} \boldsymbol{\phi}_i^{\boldsymbol{u}}\, a_i - \boldsymbol{u}_{\boldsymbol{\omega}} \right), \tag{16}$$

where the coefficients of vectors $\mathbf{E} \in \mathbb{R}^{n_{\boldsymbol{u}}}$, $\mathbf{F} \in \mathbb{R}^{n_{\boldsymbol{u}}}$, matrices $\mathbf{A} \in \mathbb{R}^{n_{\boldsymbol{u}} \times n_{\boldsymbol{u}}}$, $\mathbf{B} \in \mathbb{R}^{n_{\boldsymbol{u}} \times n_{\boldsymbol{u}}}$ and third-order tensor $\mathbf{C} \in \mathbb{R}^{n_{\boldsymbol{u}} \times n_{\boldsymbol{u}} \times n_{\boldsymbol{u}}}$ are given below.

$$\left\{ \begin{array}{lcl} A_{ij} & = & \rho \left(\boldsymbol{\phi}_j^{\boldsymbol{u}} \middle| \boldsymbol{\phi}_i^{\boldsymbol{u}} \right) \quad (= \rho\, \delta_{ij}), \\ B_{ij} & = & \rho \left(\nabla \boldsymbol{\phi}_j^{\boldsymbol{u}} \cdot \overline{\boldsymbol{u}} + \nabla \overline{\boldsymbol{u}} \cdot \boldsymbol{\phi}_j^{\boldsymbol{u}} \middle| \boldsymbol{\phi}_i^{\boldsymbol{u}} \right) + 2\eta \left(\mathrm{D}\left(\boldsymbol{\phi}_j^{\boldsymbol{u}} \right) \middle| \mathrm{D}\left(\boldsymbol{\phi}_i^{\boldsymbol{u}} \right) \right), \\ C_{ijk} & = & \rho \left(\nabla \boldsymbol{\phi}_j^{\boldsymbol{u}} \cdot \boldsymbol{\phi}_k^{\boldsymbol{u}} \middle| \boldsymbol{\phi}_i^{\boldsymbol{u}} \right), \\ E_i^{\ell} & = & \left(\chi_{\mathtt{S}}\, \boldsymbol{\lambda}^{\ell} \middle| \boldsymbol{\phi}_i^{\boldsymbol{u}} \right), \\ F_i & = & \rho \left(\nabla \overline{\boldsymbol{u}} \cdot \overline{\boldsymbol{u}} \middle| \boldsymbol{\phi}_i^{\boldsymbol{u}} \right) + 2\eta \left(\mathrm{D}\left(\boldsymbol{\phi}_j^{\boldsymbol{u}} \right) \middle| \mathrm{D}\left(\boldsymbol{\phi}_i^{\boldsymbol{u}} \right) \right) - \left(\boldsymbol{f} \middle| \boldsymbol{\phi}_i^{\boldsymbol{u}} \right). \end{array} \right. \tag{17}$$

Remark 5 (Cost reduction)**.** *The model* ROM1 *reduces the cost associated with the computation of the momentum equation (15), but the complete resolution still depends on the number of degrees of freedom of the solution due to (i) the reconstruction of the velocity field in the Uzawa iteration (16) and (ii) the projection of the Lagrange multiplier to evaluate the vector $\mathbf{E}^{\ell}$ in each inner iteration.*

3.2. Reduction of the characteristic function

To cope with the reconstruction of the full order velocity field and the projection of the Lagrange multiplier onto the velocity POD basis, we propose to

also decompose the fluctuating part of the characteristic function $\chi_{\mathsf{s}} = \overline{\chi_{\mathsf{s}}} + \widetilde{\chi_{\mathsf{s}}}$ over a POD basis $\Phi^{\chi} = (\phi_i^{\chi})_{1\leq i\leq n_T}$ truncated to n_χ modes:

$$\chi_{\mathsf{s}}(\boldsymbol{x},t) \simeq \overline{\chi_{\mathsf{s}}} + \sum_{i=1}^{n_\chi} \phi_i^{\chi}(\boldsymbol{x})\, c_i\big(\theta(t)\big), \tag{18}$$

The choice of $\overline{\chi_{\mathsf{s}}}$ is precised in the following subsection (equation (22). Notice the coefficients $(c_i)_{1\leq i\leq n_\chi}$ are parametrized by the rotation angle θ and the rotation velocity $\frac{\mathrm{d}\theta}{\mathrm{d}t}$ is imposed so that no evolution equation is needed (see subsection 3.3). Projecting the Uzawa iteration (16) over the velocity POD basis $\boldsymbol{\Phi}^{\boldsymbol{u}}$ and approximating the characteristic function as in (18) yields the following reduced Uzawa iteration

$$\widehat{\boldsymbol{\lambda}}^{\ell+1} = \widehat{\boldsymbol{\lambda}}^{\ell} + r\,\Big(\mathbf{G}\cdot\boldsymbol{a} + \mathbf{H}\cdot\boldsymbol{c} + \mathbf{L}:\boldsymbol{c}\otimes\boldsymbol{a} + \mathbf{M}\Big), \tag{19}$$

with the coefficients given below.

$$\left\{\begin{array}{lcl} \widehat{\lambda}_i^{\ell} & = & \big(\chi_{\mathsf{s}}\,\boldsymbol{\lambda}^{\ell}\big|\,\boldsymbol{\phi}_i^{\boldsymbol{u}}\big)\,, \\ G_{ij} & = & \big(\overline{\chi_{\mathsf{s}}}\,\boldsymbol{\phi}_j^{\boldsymbol{u}}\big|\,\boldsymbol{\phi}_i^{\boldsymbol{u}}\big)\,, \\ H_{ik} & = & (\phi_k^{\chi}\,(\overline{\boldsymbol{u}}-\boldsymbol{u}_{\boldsymbol{\omega}})|\,\boldsymbol{\phi}_i^{\boldsymbol{u}})\,, \\ L_{ijk} & = & \big(\phi_k^{\chi}\,\boldsymbol{\phi}_j^{\boldsymbol{u}}\big|\,\boldsymbol{\phi}_i^{\boldsymbol{u}}\big)\,, \\ M_i & = & (\overline{\chi_{\mathsf{s}}}\,(\overline{\boldsymbol{u}}-\boldsymbol{u}_{\boldsymbol{\omega}})|\,\boldsymbol{\phi}_i^{\boldsymbol{u}})\,. \end{array}\right. \tag{20}$$

Due to the iterative procedure for updating the Lagrange multiplier $\boldsymbol{\lambda}$, the *reduced Lagrange multiplier* $\widehat{\boldsymbol{\lambda}}^{\ell} = (\widehat{\lambda}_i^{\ell})_{1\leq i\leq n_{\boldsymbol{u}}}$ can be directly used in place of $\mathbf{E}^{\ell}$ in the reduced momentum equation (15):

$$\mathbf{A}\cdot\frac{\mathrm{d}\boldsymbol{a}}{\mathrm{d}t} + \mathbf{B}\cdot\boldsymbol{a} + \mathbf{C}:\boldsymbol{a}\otimes\boldsymbol{a} + \widehat{\boldsymbol{\lambda}}^{\ell} + \mathbf{F} = \mathbf{0}. \tag{21}$$

The reduced momentum equation (21) along with the reduced Uzaw iteration (19) constitute the proposed low order dynamical system, referred as ROM2.

3.3. Parametrization of the characteristic function

Now, we shall build explicit evaluations of the coefficients $\boldsymbol{c}(\theta)$ for characteristic function. In practical applications, the rotating solids (fans, agitators) usually exhibit some rotational symmetries that can be exploited. Denote θ_{s}

the *angular period* defined as the minimum angle such that $\chi_{\mathtt{s}} = R(\theta_{\mathtt{s}})\chi_{\mathtt{s}}$ with $R(\theta)$ the rotation by angle θ about the imposed rotation axis $\boldsymbol{e}_\omega$, so that the $c_i : [0, \theta_{\mathtt{s}}] \to \mathbb{R}$, $1 \leq i \leq n_\chi$ are periodic functions $c_i(0) = c_i(\theta_{\mathtt{s}})$. In this work, we propose the use of periodic piecewise polynomial interpolators (periodic splines), built as follows.

Remark 6 (Mean characteristic function)**.** *In this work, the reference field* $\overline{\chi_{\mathtt{s}}} : \Omega \to [0, 1]$ *in (18) is defined as the mean of the characteristic function over a partial rotation of angle* $\theta_{\mathtt{s}}$*:*

$$\overline{\chi_{\mathtt{s}}}(\boldsymbol{x}) = \frac{1}{\theta_{\mathtt{s}}} \int_0^{\theta_{\mathtt{s}}} R(\theta)\chi_{\mathtt{s}}(\boldsymbol{x}, 0)\, \mathrm{d}\theta. \tag{22}$$

The reference coefficients $c_i(\theta_n)$, $1 \leq i \leq n_\chi$ are defined as the projection of the fluctuating part of the characteristic function over its POD basis Φ^χ for a set of selected angles $(\theta_n)_{1 \leq n \leq N-1}$ taken in the angular period $\theta_n \in [0, \theta_{\mathtt{s}}]$:

$$c_i(\theta_n) = \left(R\big(\theta_n\big)\chi_{\mathtt{s}}(\boldsymbol{x}, 0) - \overline{\chi_{\mathtt{s}}}(\boldsymbol{x})\middle|\, \phi_i^\chi(\boldsymbol{x})\right), \quad 1 \leq i \leq n_\chi. \tag{23}$$

The set D_i of $N_i + 1$ data points used to build the interpolator for the i-th coefficient is

$$D_i \triangleq \big[\big(\theta_0, c_i(\theta_0)\big), \cdots, \big(\theta_{N_i}, c_i(\theta_{N_i})\big)\big], \tag{24}$$

with $0 = \theta_0 < \cdots < \theta_n < \cdots < \theta_{N_i} = \theta_{\mathtt{s}}$. The associated interpolant $S_i \simeq c_i$ on the domain $\Theta = [\theta_0, \theta_{N_i}]$ is such that $S_i(\theta) = P_{i,n}(\theta)$, $\forall \theta \in (\theta_n, \theta_{n+1})$ where the $P_{i,n}(\theta)$, $0 \leq n \leq N_i - 1$ are third order polynomials that fulfill the following constraints:

(C1)	$P_{i,n}(\theta_n) = P_{i,n-1}(\theta_n) = c_i(\theta_n)$,	$1 \leq n \leq N_i - 1$,	(C^0 interpolator);
(C2)	$P'_{i,n}(\theta_n) = P'_{i-1}(\theta_n)$,	$1 \leq n \leq N_i - 1$,	(C^1 interpolator);
(C3)	$P''_{i,n}(\theta_n) = P''_{i-1}(\theta_n)$,	$1 \leq n \leq N_i - 1$,	(C^2 interpolator);
(C4)	$P_{i,0}(\theta_0) = P_{i,N_i}(\theta_{N_i})$,		(periodic);
(C5)	$P'_{i,0}(\theta_0) = P'_{i,N_i}(\theta_{N_i})$,		(periodic);
(C6)	$P''_{i,0}(\theta_0) = P''_{i,N_i}(\theta_{N_i})$,		(periodic).

The $N_i + 1$ interpolation points for the i-th coefficient can be selected by a greedy approach, as detailed in appendix Appendix B. Finally, we define the

multi-valued function $\boldsymbol{S}(\theta) = \big(S_1(\theta), \cdots, S_{n_\chi}(\theta)\big)$ so that the reduced Uzawa iteration (19) reads:

$$\widehat{\boldsymbol{\lambda}}^{\ell+1} = \widehat{\boldsymbol{\lambda}}^{\ell} + r\,\Big(\mathbf{G}\cdot\boldsymbol{a} + \mathbf{H}\cdot\boldsymbol{S}(\theta) + \mathbf{L} : \boldsymbol{S}(\theta)\otimes\boldsymbol{a} + \mathbf{M}\Big), \tag{25}$$

with the vectors, matrices and third order tensor defined in (20).

4. Interpolation of the reduced order models

The POD approach yields reduced order models that lack robustness with respect to changes in the parametric configuration (see *e.g.* [27] for a parametric analysis in the context of turbomachinery and [34] for a mathematical a priori estimate in the context of CFD). Among the numerous approaches considered to circumvent the costly simulation of the HDM needed to derive the POD-ROM for a new parameter, the most appealing are based on some kind of *interpolation* (see *e.g.* [35] and references therein). In this work, we focus on a robust interpolation method proposed in [38], namely, the IDW-G method which is based on the geometry of the Grassmann manifold. First, we motivate and recall the historical Grassmannian interpolation method developed in [36, 37]. Second, we recall the IDW-G algorithm. Third, we sketch the use of this method to interpolate the POD-ROMs proposed in the previous section 3.

4.1. Interpolation over the Grassmann Manifold

Denote by $\boldsymbol{\Phi} = (\Phi_i)_{1\leq i\leq n_p}$ the set of POD bases obtained from the simulation of the HDM for the set of parameters $\mathrm{P} = (p_i)_{1\leq i\leq n_p}$, and $p^\star \notin \mathrm{P}$ the new parameter for which we want to construct one of the POD-ROM presented in section 3. It has been shown that the construction of the POD-ROM involves the (weighted) euclidian projection of the governing equation over the POD basis. On the other hand, it is well known that the projection onto the subspace $V_i = \mathrm{span}\,(\Phi_i)$ does not depend on the chosen basis used to describe it:

$$\pi_\Phi(\mathbf{U}) = \pi_{\Phi\cdot\mathbf{M}}(\mathbf{U}), \quad \forall \mathbf{M}\in O(m), \tag{26}$$

where $\pi_\Phi(\bullet) = \Phi \cdot^\intercal \Phi \cdot \bullet$ is a projection operator and $O(m)$ is the set of square orthogonal matrices of size m. Thus, we seek for a method to interpolate the set $(V_i)_{1\leq i\leq n_p}$ of m-dimensional subspaces of $\mathbb{R}^n$, that is, to realize an interpolation in the space $G_m(\mathbb{R}^n) = \{\mathbf{M} \in \mathbb{R}^{n\times m};\ {}^\intercal\mathbf{M} \cdot \mathbf{M} = \boldsymbol{I}\}$ known as the *Grassmann manifold* (see *e.g.* [41]). The subspaces $(V_i)_{1\leq i\leq n_p}$ are associate with the equivalence classes of all their bases, and form a set of points on $G_m(\mathbb{R}^n)$. In [37], the authors propose to cope with the difficulty to interpolate over a manifold as follows. First, the sample (subspaces engendered by the) POD bases are sent to the tangent space of $G_m(\mathbb{R}^n)$ at a given reference point $\text{span}\,(\Phi_r)$ through the *geodesic logarithm*, which expression is [41, 37]

$$\begin{array}{rcl} \log_{\Phi_r}(\Phi_i) & = & \mathbf{U} \cdot \arctan(\mathbf{\Sigma}) \cdot^\intercal \mathbf{V} \cdot ({}^\intercal\Phi_i \cdot \Phi_i)^{\frac{1}{2}}, \quad \forall i \in [1, \cdots, n_p], \\ \text{with}\ \ \mathbf{U} \cdot \mathbf{\Sigma} \cdot^\intercal \mathbf{V} & = & \text{SVD}\left(\left(\Phi_i \cdot ({}^\intercal\Phi_r \cdot \Phi_i)^{-1} - \Phi_r\right) \cdot ({}^\intercal\Phi_r \cdot \Phi_r)^{\frac{1}{2}} \right). \end{array} \tag{27}$$

Second, the images are interpolated by any standard method suitable for vector space. Third, the resulting interpolation is sent back on the manifold through the geodesic exponential map which expression is [41, 37]

$$\begin{array}{rcl} \exp_{\Phi_r}(\mathbf{\Gamma}) & = & \left(\Phi_r \cdot ({}^\intercal\Phi_r \cdot \Phi_r)^{\frac{1}{2}} \cdot \mathbf{V} \cdot \cos(\mathbf{\Sigma}) + \mathbf{U} \cdot \sin(\mathbf{\Sigma})\right) \cdot^\intercal \mathbf{V} \cdot ({}^\intercal\Phi_r \cdot \Phi_r)^{\frac{1}{2}}, \\ \text{with}\ \ \mathbf{U} \cdot \mathbf{\Sigma} \cdot^\intercal \mathbf{V} & = & \text{SVD}\left(\mathbf{\Gamma} \cdot ({}^\intercal\Phi_r \cdot \Phi_r)^{\frac{1}{2}}\right). \end{array} \tag{28}$$

Remark 7 (Well posed interpolation)**.** *It is assumed that* $\det({}^\intercal\Phi_r \cdot \Phi_i) \neq 0$, $\forall i \in \{1, \cdots, n_p\}$.

Remark 8 (Dependence on the reference point)**.** *The method from [37] recalled above depends on the choice of the reference point. This could impacts the robustness of the interpolation. To circumvent this drawback, we focus propose to use the IDW-G interpolation method from [38] which we recall below.*

4.2. Inverse Distance Weighting

In this paper, we also consider the Inverse Distance Weighting interpolation over the Grassmann manifold (IDW-G) proposed in [38]. The advantage of this method compared with the standard interpolation [37] recalled in the previous

section is that it does not rely on the choice of a reference point at which the tangent space is constructed. The IDW-G method solves the following minimization problem:

$$(\mathcal{P}_{\boldsymbol{p}}) \begin{cases} \text{For} \quad p \in \mathbb{R}, \quad \text{find} \quad \Phi^{\mathtt{I}} \in G_m(\mathbb{R}^n) \quad \text{s.t.} \quad : \\ \Phi^{\mathtt{I}}(p) = \underset{\Phi \in G_m(\mathbb{R}^n)}{\arg\min} \left(\frac{1}{2} \sum_{i=1}^{n_p} \alpha_i(p) \ \left(d_G(\Phi, \Phi_i) \right) \right)^2, \end{cases} \tag{29}$$

where d_G is the geodesic distance and the weights $(\alpha_i(\lambda))_{i=1}^N$ verify $\sum_{i=1}^N \alpha_i(\lambda) = 1$.
The method relies on the following constructive theorem from [38].

Theorem 1 (IDW-G sequence)**.** *If the $\Phi_1, \cdots, \Phi_{n_p}$ are all contained in the ball $B(\Phi^*, r)$ where $\Phi^* \in G_m(\mathbb{R}^n)$ and $r < \frac{\pi}{4\sqrt{2}}$, then for all $p \in \mathbb{R}$, the problem $(\mathcal{P}_p)$ admits a unique solution $\Phi^{\mathtt{I}}$ in $B(\Phi^*, r)$. Moreover, for all initial $\widehat{\Phi} \in B(\Phi^*, r)$, the sequence $\left(\Phi_\ell^{\mathtt{I}}\right)_{\ell \in \mathbb{N}}$ defined by:*

$$\Phi_0^{\mathtt{I}} = \widehat{\Phi}; \qquad \Phi_{\ell+1}^{\mathtt{I}} = \exp_{\Phi_\ell^{\mathtt{I}}} \left(\frac{1}{2n_p} \sum_{i=1}^{n_p} \alpha_i(p) \exp_{\Phi_\ell^{\mathtt{I}}}^{-1}(\Phi_i) \right) \tag{30}$$

converges to $\Phi^{\mathtt{I}}$.

In practice, convergence is assumed when the norm of the gradient of the functional associated with the problem $\mathcal{P}_p$ is below a predefined threshold (see [38]). This sequence yields the algorithm 2.

4.3. Interpolation of the low-order dynamical systems

The set of non-dimensional parameters involved in the full-order model are classically the Reynolds number and some shape parameters for the rotating solid. Additionally, the POD-ROMs presented in section 3 involve the following bases:

ROM1: POD basis for the velocity $\boldsymbol{\Phi}^{\boldsymbol{u}}$ only,

ROM2: POD bases for the velocity $\boldsymbol{\Phi}^{\boldsymbol{u}}$ and the characteristic function Φ^{χ}.

In this work, we focus on the interpolation over a set of Reynolds number (related with the solid rotation velocity). This situation arises in most industrial

Data: Sets of parameters $(p_n)_{1\leq n\leq n_p}$ with associated POD bases $(\Phi_n)_{1\leq n\leq n_p}$, exponent α, residual tolerance ϵ_{tol} and target parameter $p^\star$.

Result: Interpolated basis $\Phi^{\mathtt{I}} \simeq \Phi^\star$.

$r = \underset{i\in[1,n_p]}{\text{argmin}} |p^\star - p_i|$ // Select initial value ;

$\ell = 0$;

$\Phi^{\mathtt{I}}_\ell = \Phi_r$;

$S = \sum_{i=1}^{n_p} \dfrac{1}{\parallel p^\star - p_i \parallel^\alpha}$ // Sum of inverse distance weights ;

for $i \in [1, n_p]$ **do**

  $w_i = \dfrac{1}{S \parallel p^\star - p_i \parallel^\alpha}$ // Normalized inverse distance weights ;

end

$\epsilon = \infty$;

while $\epsilon >$ tol **do**

  $\ell = \ell + 1$;

  for $i \in [1, n_p]$ **do**

    $\boldsymbol{\Gamma}_i = \log_{\Phi^{\mathtt{I}}_{\ell-1}}(\Phi_i)$ // Send to the tangent plane at $\Phi^{\mathtt{I}}_{\ell-1}$;

  end

  $\boldsymbol{\Gamma}^{\mathtt{I}}_\ell = \frac{1}{2n_p} \sum_{i=1}^{n_p} w_i \boldsymbol{\Gamma}_i$ // Weighted average;

  $\Phi^{\mathtt{I}}_\ell = \exp_{\Phi^{\mathtt{I}}_{\ell-1}}(\boldsymbol{\Gamma}^{\mathtt{I}}_\ell)$ // Go back on the manifold;

end

$\Phi^{\mathtt{I}} = \Phi^{\mathtt{I}}_\ell$ // Select solution ;

Algorithm 2: Interpolation of POD bases by the IDW-G method from [38], where $\parallel \bullet \parallel$ denotes the euclidean norm. Closed-form expressions for the geodesic logarithm $\log_\Phi : G_m(\mathbb{R}^n) \to T_\Phi G_m(\mathbb{R}^n)$ and the geodesic exponential $\exp_\Phi : T_\Phi G_m(\mathbb{R}^n) \to G_m(\mathbb{R}^n)$ over the Grassmann manifold are given in (27) and (28), respectively.

cases for which the installation geometry is fixed and only the fans/agitators rotation velocity is controlled. In those cases, there is no need to interpolate the

POD bases for the characteristic function which can be determined once for all along with the spline approximation $(S_i)_{1\leq i\leq n_\chi}$ defined in subsection 3.3 before the construction of the ROM2.

In order to interpolate the POD bases for the velocity as described in the previous subsection (algorithm 2), the velocity POD bases have to be orthonormal with respect to the scalar product of $\mathbb{R}^n$. However, the scalar product of L^2 is used to construct the *snapshot* correlation matrices from which the POD bases are derived so that the POD bases are orthogonal in L^2. In that case, the sample bases must be orthonormalized in $\mathbb{R}^n$ before the interpolation, and the interpolated basis must be orthonormalized back in L^2, *e.g.* with a Gram-Schmidt procedure.

Finally, the proposed POD-ROMs involve the mean fields for the velocity and the characteristic function. Since we do not identify a special interpolation space, they are interpolated by a cubic spline applied on the matrices coefficients.

5. Numerical results

This section is devoted to illustrate the performances of the proposed methods through numerical results. First, we describe the academic configuration used in the tests. Second, we show the benefit of the two reduced order models proposed in section 3. Third, we show the results for the interpolation method describe in previous section 4. All the numerical tests have been performed using the Python/C++ finite element library DOLFIN [42] on a computer with 32 cores and 64Go of RAM.

5.1. Description of the configuration

We consider a circular spatial domain $\Omega = \Omega_{\mathtt{S}} \cup \Omega_{\mathtt{F}}$ $(d = 2)$ filled with a rotating ellipsoidal solid $\Omega_{\mathtt{S}}$ immersed in an incompressible newtonian fluid $\Omega_{\mathtt{F}}$ (see figure 2a). The domain radius is 1m, the ellipse principal radius is $R = 0.5$m

with an aspect ratio of 0.2. In the sequel, the Reynolds number associated with this configuration is defined as

$$\mathrm{Re} = \frac{\rho U L}{\eta}, \tag{31}$$

with the density $\rho = 1$ (kg.m^{-3}), the dynamic viscosity $\eta = 0.01$ (kg.m^{-1}.s^{-1}), the reference velocity $U = R\,\frac{\mathrm{d}\theta}{\mathrm{d}t}$ (m.s^{-1}) and $L = 2R$ (m) the ellipse principal diameter.

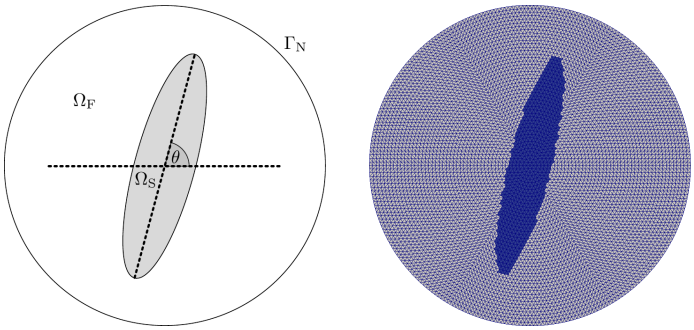

(a) Schematic (b) Non-conforming mesh

Figure 2: Academic configuration used for the numerical test.

The finite element mesh includes 52669 nodes and is not conforming with the solid boundaries (see figure 2b). The boundary condition on $\partial\Omega = \Gamma_N$ is outflow ($\boldsymbol{\sigma}_F \cdot \boldsymbol{n} = 0$). The momentum equation and the continuity equation are solved together by a monolithic formulation for which the finite element spaces are chosen as the linear vector Lagrange elements enriched with the cubic vector bubble elements for the velocity and piecewise linear elements for the pressure. This mixed finite element space is known as the *mini space* (see [43] for details). The time-step for temporal discretization is fixed to 1ms. The parameters for Uzawa iterations (see section 2.3) are $r = 10^3$ and $\epsilon_{\mathrm{tol}} = 10^{-3}$. For this setting, an average of $\ell = 6$ Uzawa iterations are needed to achieve convergence of the velocity in the solid domain. The average computational time for each Uzawa iteration of the high-dimensional model is $5,2$s.

5.2. Comparison between HDM and proposed POD-ROMs

The configuration described in previous subsection is used for the simulation of the HDM with a zero initial condition. In this subsection, the Reynolds number (31) is fixed to Re = 1000. The POD is classically applied to ergodic processes for which the statistical and temporal averages coincide. Thus, we first present the results obtained for a steady periodic flow. Second, the results for the transient period are shown.

5.2.1. Steady Periodic flow

We first run the HDM simulation for a transient period of $7,5$s. Second, $n_T = 150$ regularly spaced snapshots are exported over a period of $T = 0,75$s to construct the POD basis for the velocity $\mathbf{\Phi}^{\boldsymbol{u}}$ (figure 3).

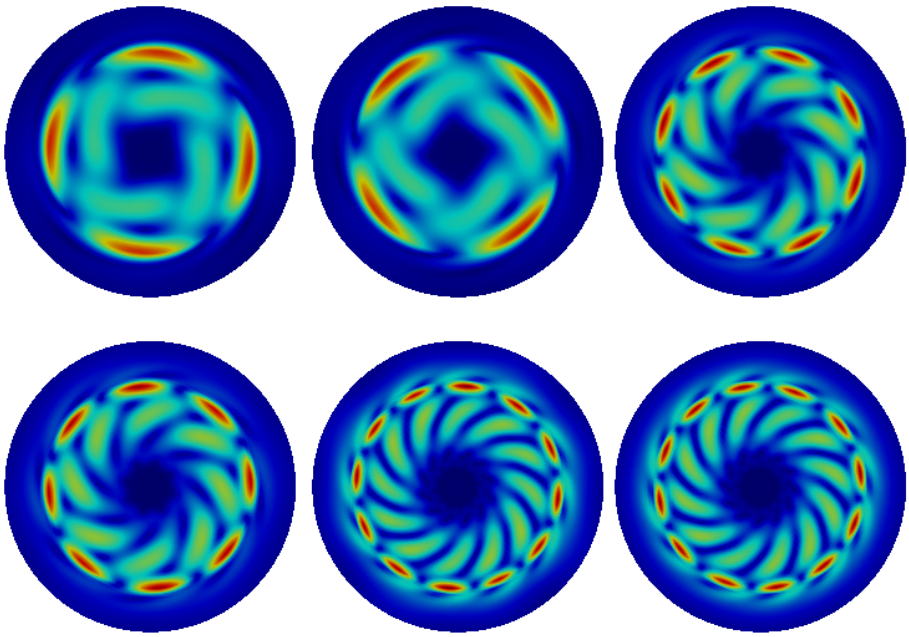

Figure 3: First modes for velocity $(\boldsymbol{\phi}_i^{\boldsymbol{u}})_{1\leq i\leq 6}$ in the steady case (from left to right and top to bottom).

The eigen-values $(\lambda_i)_{1\leq i\leq n_T}$ of the correlation matrices (A.8) associated with the velocity and the characteristic function are shown in figure 5a. The figure 5b

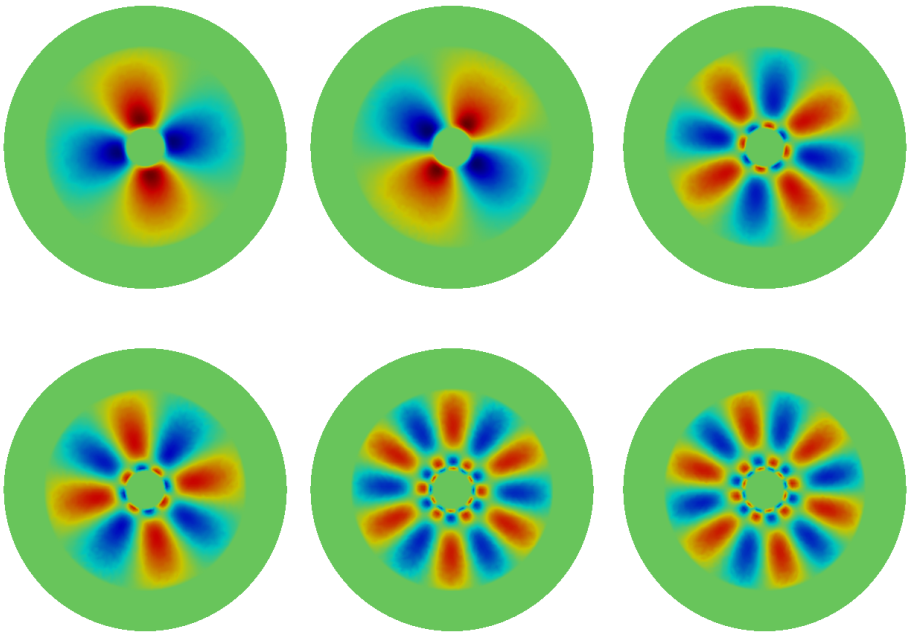

Figure 4: First modes for characteristic function $(\phi_i^\chi)_{1\leq i\leq 6}$ for both the steady and the transient cases (from left to right and top to bottom).

shows the associated *reconstruction error* computed from the eigen values as

$$E(n) = 1 - \frac{\sum_{i=n+1}^{n_T} \lambda_i}{\sum_{j=1}^{n_T} \lambda_j}. \tag{32}$$

We select $n_{\boldsymbol{u}} = 30$ modes for the velocity and $n_\chi = 35$ modes for the characteristic function in order to capture 99.9% of the snapshots information. The time-step for the POD-ROMs is 5ms, and the parameters for the Uzawa algorithm are $r = 100$ and $\epsilon_{\text{tol}} = 10^{-3}$.

The periodic spline interpolation in ROM2 of the angular coefficients for the characteristic function described in subsection 3.3 is build over the angular period $\theta_{\text{S}} = \pi$ rad from a data set of $N^\star = 1000$ angles in $[0, \theta_{\text{S}}]$ and a relative

tolerance on the periodic spline reconstruction of $\varepsilon_\theta = 10^{-3}$. The computational

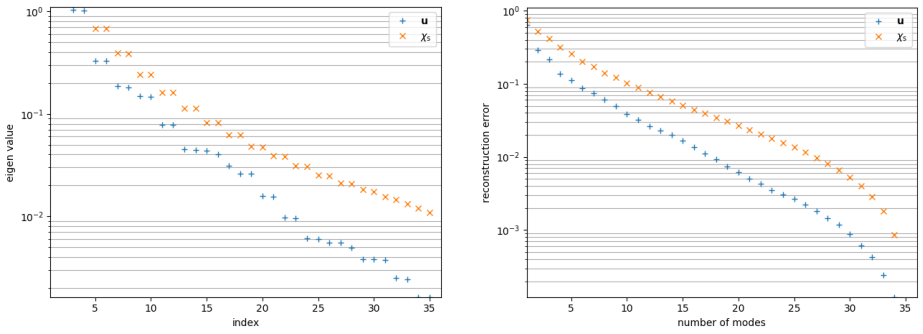

(a) Eigen-values (b) Relative-information content

Figure 5: Eigen-values (left) of the temporal correlation matrix (A.8) and reconstruction error (32) associated with the velocity field $\boldsymbol{u}$ (+) and the solid characteristic function χ_S (×).

times are detailed in table 1 in which the advantage of the ROM2 over the ROM1 is clearly visible. The fluctuating velocity for the three models (HDM, ROM1 and ROM2) is shown in figure 6. The reconstructions provided by both the ROM1 and the ROM2 are very close to the HDM, despite some artifacts associated with the truncation of the POD basis. These results are reflected in the vorticity shown in figure 7, where we see the tiny vortices at the ellipse tips are well reconstructed. Finally, the temporal coefficients associated with the first six POMs of the velocity are shown in Appendix C, figure C.12 for the three models. A detailed comparison of the error on these coefficients is shown in figure 8. We see that despite the characteristic function for the solid is approximated, both models yields similar results.

5.2.2. Transient flow

Here, we apply the proposed method on the transient period. That is, we start the simulation from a zero initial condition and consider 200 snapshots over a rotation of the ellipsoidal body by an angle of $\theta = \pi$. The Reynolds number (31) is still $\mathrm{Re} = 1000$ as in the previous subsection. We fix the threshold on the RIC to 99%, which yields 45 POMs for the velocity. Since the geometry

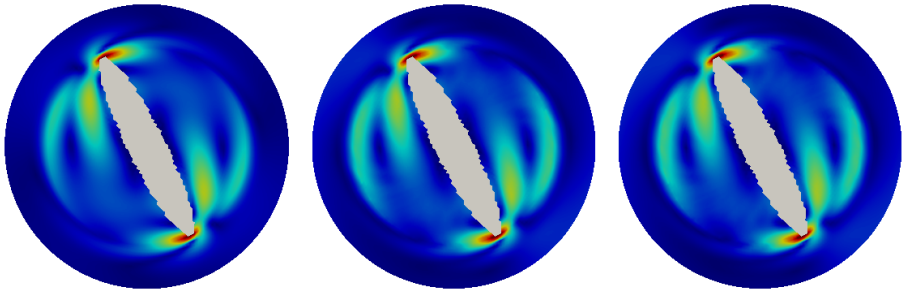

Figure 6: Magnitude of the fluctuating velocity $\boldsymbol{u}(\boldsymbol{x},t)-\overline{\boldsymbol{u}}(\boldsymbol{x})$. Left: HDM. Middle: ROM1. Right: ROM2.

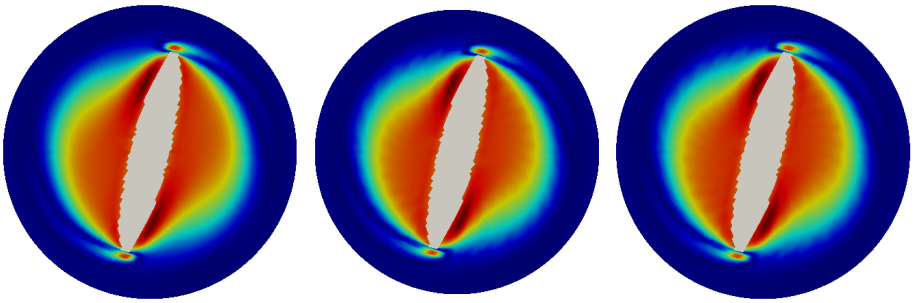

Figure 7: Magnitude of vorticity. Left: HDM. Middle: ROM1. Right: ROM2.

is the same as in the previous case, the number of POMs for the characteristic function is still 35. Again, the reconstructions of the velocity from the proposed ROM1 and ROM2 are very close to the HDM with some discrepancies due to (i) the coarse grid and (ii) the truncation in the POMs. The temporal coefficients for the first six POMs for the velocity are shown in Appendix C, figure C.13 and a detailed comparison of the error on these coefficients is shown in figure 10. We see the temporal evolution of the dominant modes is conform with the HDM for both the ROM1 and the ROM2.

	Uzawa iteration	Total
HDM	5.2s	7h 34m 53s
ROM1	0.6s	19m 36s
ROM2	0.01s	21s

Table 1: Computational times for the HDM, ROM1 and ROM2. Notice the time step is 1ms for the HDM and 5ms for the POD-ROMs and parameters for the Uzawa algorithm differ leading to an average of 6 iterations for the HDM and 10 iterations for the POD-ROMs.

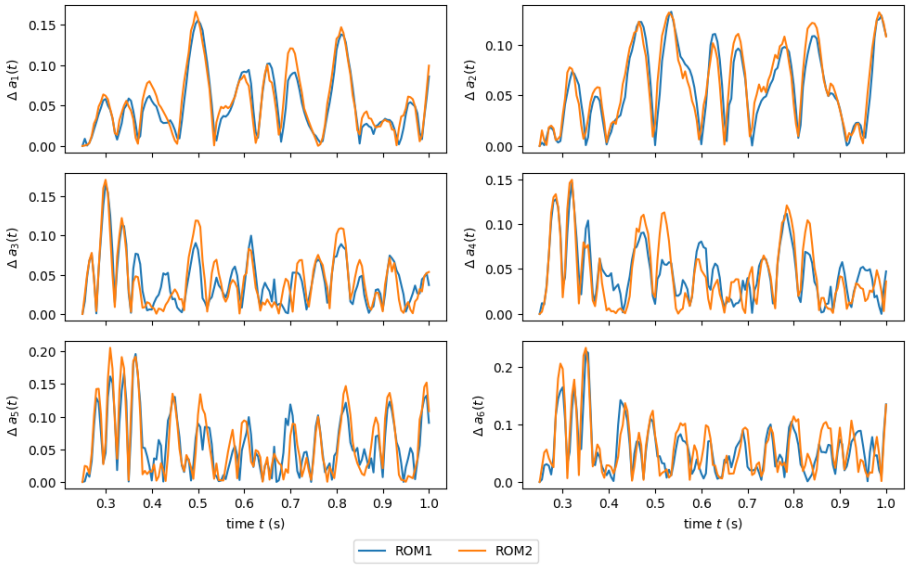

Figure 8: Temporal evolution of the coefficients for the fluctuating part of the velocity in the transient case (see section 5.2.1). The coefficients for the HDM are obtained by projection of the snapshots over the POD modes $a_i(t) = (\boldsymbol{u}_h(\boldsymbol{x},t)|\,\boldsymbol{\phi}_i^{\boldsymbol{u}}(\boldsymbol{x}))$. The coefficients for the ROM1 and the ROM2 are obtained from the solution of (15) and (21), respectively.

5.3. Comparison between the direct and interpolated ROM2

In this section, we show the results of the ROM2 obtained from the interpolation of POMs with respect to the Reynolds number (31) by the IDW-G method (algorithm 2). First, we build the POMs and the ROM2 from a direct simulation at $p^\star = 1250$. This will be used a reference (thus labeled ref) to which the interpolated POMs and ROM2 are compared. Second, we build

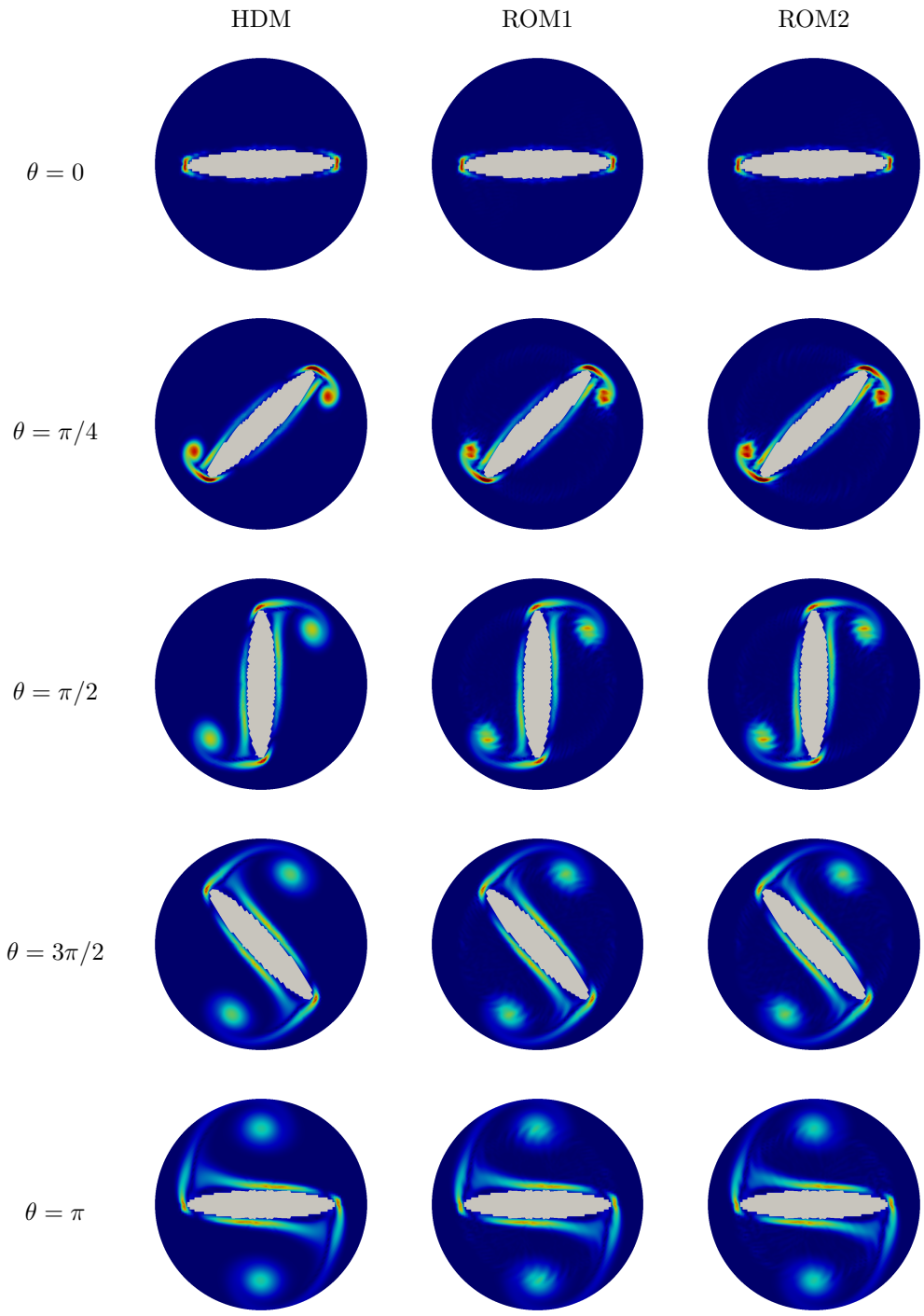

Figure 9: Magnitude of vorticity (transient period, see section 5.2.2).

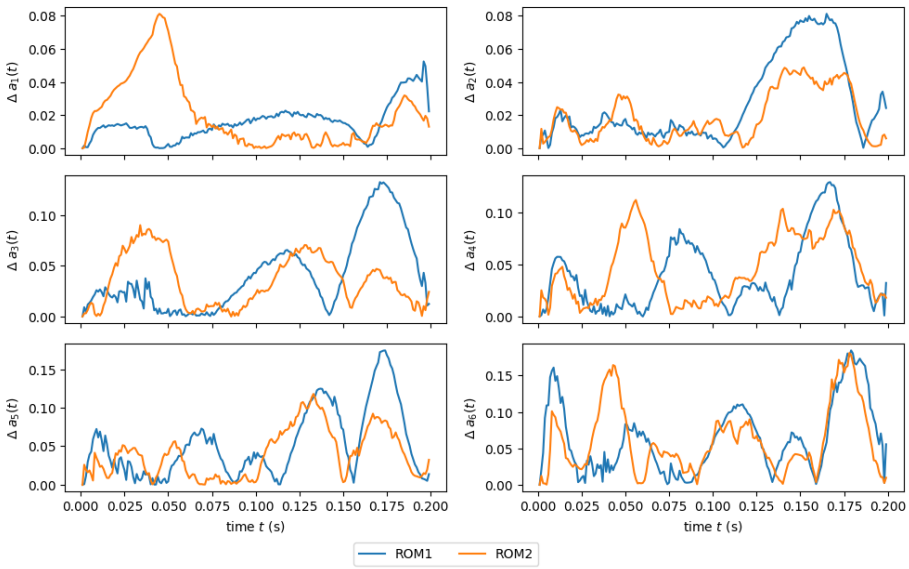

Figure 10: Temporal evolution of the coefficients for the fluctuating part of the velocity during the transient period (see section 5.2.2). The coefficients for the HDM are obtained by projection of the snapshots over the POD modes $a_i(t) = (\boldsymbol{u}_h(\boldsymbol{x},t)|\,\boldsymbol{\phi}_i^{\boldsymbol{u}}(\boldsymbol{x}))$. The coefficients for the ROM1 and the ROM2 are obtained from the solution of (15) and (21), respectively.

the POMs associated with the parameters $p \in [1000, 1150, 1350, 1500]$ and we interpolate at $p^\star$ by two methods: (i) a naive method (vectorial interpolation of the POMs coefficients by a piecewise linear interpolator) which we label vec and by the method described in algorithm 2, section 4 with exponent $\alpha = 2$ and tolerance $\epsilon_{\text{tol}} = 10^{-9}$ which we label idw. The Grassmann distance between the reference and both interpolation are:

$$\begin{aligned} d(\boldsymbol{\Phi}^{\boldsymbol{u}}_{\text{ref}}, \boldsymbol{\Phi}^{\boldsymbol{u}}_{\text{vec}}) &= 2.06, \\ d(\boldsymbol{\Phi}^{\boldsymbol{u}}_{\text{ref}}, \boldsymbol{\Phi}^{\boldsymbol{u}}_{\text{idw}}) &= 1.56. \end{aligned} \tag{33}$$

Recall the injectivity radius for the exponential map on the Grassmann manifold is $\frac{\pi}{2}$, so that the basis $\boldsymbol{\Phi}^{\boldsymbol{u}}_{\text{vec}}$ is unreliable. This is reflected in the reconstruction error:

$$\begin{aligned} \| \mathbf{U}_{\text{ref}} - \mathbf{U}_{\text{vec}} \|_{\text{F}} &= 235.44, \\ \| \mathbf{U}_{\text{ref}} - \mathbf{U}_{\text{idw}} \|_{\text{F}} &= 82.01, \end{aligned} \tag{34}$$

where $[\mathbf{U}]_{i,j} = \sum_{n=1}^{n_{\boldsymbol{u}}} a_n(t_j)\, \boldsymbol{\phi}_n^{\boldsymbol{u}}(\boldsymbol{x}_i)$ and $\| \bullet \|_{\mathrm{F}}$ denotes the Froebenius norm. Finally, wee show in Appendix C, figure C.14 the temporal coefficients for the POMs associated with the velocity obtained by the ROM2 build from the reference and both interpolated bases. The error between the reference and the interpolated ROM2 are shown in figure 11

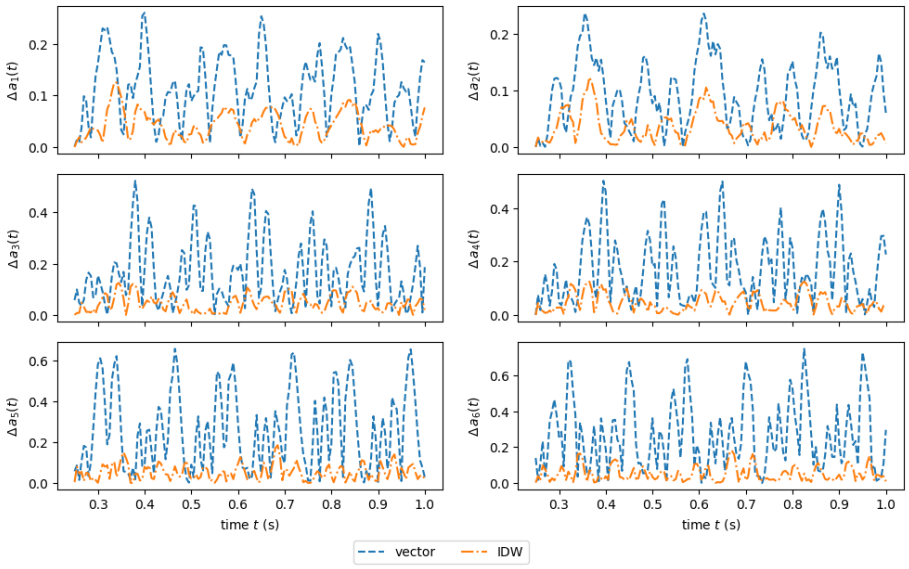

Figure 11: Temporal evolution of the coefficients for the fluctuating part of the velocity in the interpolation case (see section 5.3). The coefficients for the HDM are obtained by projection of the snapshots over the POD modes $a_i(t) = \left(\boldsymbol{u}_h(\boldsymbol{x},t) | \, \boldsymbol{\phi}_i^{\boldsymbol{u}}(\boldsymbol{x})\right)$. The coefficients for the ROM1 and the ROM2 are obtained from the solution of (15) and (21), respectively.

6. Conclusion

We have proposed a POD-based reduced order model for flow induced by rigid solids in forced rotation that substantially reduces the computational cost compared to previous approaches, while maintaining a high precision compared to the results obtained from the high dimensional model or from the standard POD-ROM. The method is non-intrusive, and thus widely applicable. Additionally, it proves compatible with state of the art adaptive method to avoid

the computational cost associated with the production of the snapshots for each new parameter.

The high number of modes needed to achieve a prescribed reconstruction error could be reduced by considering a rotational frame, mapping each snapshot to a reference frame. This is the subject of a work in progress. Also, a parametric exploration of the effects of the solid geometry on the flow should be performed by interpolation also with respect to the geometric parameters.

References

[1] E. H. Dowell, Modeling of Fluid-Structure Interaction, Springer International Publishing, 2015, Ch. 9, pp. 439–478.

[2] S. L. Dixon, C. Hall, Fluid mechanics and thermodynamics of turbomachinery, Butterworth-Heinemann, 2013.

[3] R. N. Pinto, A. Afzal, L. V. D'Souza, Z. Ansari, A. D. M. Samee, Computational fluid dynamics in turbomachinery: a review of state of the art, Archives of Computational Methods in Engineering 24 (3) (2017) 467–479.

[4] J. Denton, Some limitations of turbomachinery cfd, in: ASME Turbo Expo 2010: Power for Land, Sea, and Air, American Society of Mechanical Engineers, 2010, pp. 735–745.

[5] F. Montomoli, M. Carnevale, A. D'Ammaro, M. Massini, S. Salvadori, Limitations in Turbomachinery CFD, Springer International Publishing, 2015, pp. 21–32.

[6] G. Hou, J. Wang, A. Layton, Numerical methods for fluid-structure interaction–a review, Communications in Computational Physics 12 (2) (2012) 337–377.

[7] G. Houzeaux, R. Codina, A chimera method based on a dirichlet/neumann (robin) coupling for the navier–stokes equations, Computer Methods in Applied Mechanics and Engineering 192 (31-32) (2003) 3343–3377.

[8] C. A. Felippa, T. L. Geers, Partitioned analysis for coupled mechanical systems, Engineering Computations 5 (2) (1988) 123–133.

[9] R. Glowinski, T.-W. Pan, T. I. Hesla, D. D. Joseph, J. Periaux, A fictitious domain method with distributed lagrange multipliers for the numerical simulation of particulate flow, Contemporary mathematics 218 (1998) 121–137.

[10] R. Glowinski, T.-W. Pan, T. I. Hesla, D. D. Joseph, A distributed lagrange multiplier/fictitious domain method for particulate flows, International Journal of Multiphase Flow 25 (5) (1999) 755–794.

[11] N. A. Patankar, P. Singh, D. D. Joseph, R. Glowinski, T.-W. Pan, A new formulation of the distributed lagrange multiplier/fictitious domain method for particulate flows, International Journal of Multiphase Flow 26 (9) (2000) 1509–1524.

[12] S. Court, M. Fournié, A. Lozinski, A fictitious domain approach for fluid-structure interactions based on the extended finite element method., ESAIM: Proceedings and Surveys 45 (2014) 308–317.

[13] E. Hachem, Stabilized finite element method for heat transfer and turbulent flows inside industrial furnaces, Ph.D. thesis, MINES ParisTech, France (2009).

[14] E. Hachem, S. Feghali, R. Codina, T. Coupez, Immersed stress method for fluid–structure interaction using anisotropic mesh adaptation, International Journal for Numerical Methods in Engineering 94 (9) (2013) 805–825.

[15] R. P. Fedkiw, T. Aslam, B. Merriman, S. Osher, A non-oscillatory eulerian approach to interfaces in multimaterial flows (the ghost fluid method), Journal of computational physics 152 (2) (1999) 457–492.

[16] E. A. Fadlun, R. Verzicco, P. Orlandi, J. Mohd-Yusof, Mohd-Yusof, Combined immersed-boundary finite-difference methods for three-dimensional complex flow simulations, Journal of computational physics 161 (1) (2000) 35–60.

[17] B. I. Epureanu, K. C. Hall, E. H. Dowell, Reduced-order models of unsteady viscous flows in turbomachinery using viscous–inviscid coupling, Journal of Fluids and Structures 15 (2) (2001) 255–273.

[18] P. G. Tucker, Computation of unsteady turbomachinery flows: Part 1 – progress and challenges, Progress in Aerospace Sciences 47 (7) (2011) 522–545.

[19] P. Holmes, C. W. Rowley, G. Berkooz, J. L. Lumley, Turbulence, coherent structures, dynamical systems and symmetry (1st Edition), Cambridge university press, 1996.

[20] D. D. Kosambi, Statistics in function space, Journal of the Indian Mathematical Society 7 (1943) 76–88.

[21] K. Karhunen, Zur spektraltheorie stochastischer prozesse, Annales Academiae Scientiarum Fennicae, Series A1 34.

[22] M. Loève, Fonctions aléatoires du second ordre, Appendix to the book of P. Lévy: Processus stochastiques et mouvement Brownien, Gauthier-Villars Paris (1948) 299–352.

[23] M. Loève, Probability theory: foundations, random sequences, van Nostrand Princeton, NJ, 1955.

[24] K. E. Willcox, J. D. Paduano, J. Peraire, K. C. Hall, Low order aerodynamic models for aeroelastic control of turbomachines, in: 40th Structures, Structural Dynamics, and Materials Conference and Exhibit, 1999.

[25] K. E. Willcox, Reduced-order aerodynamic models for aeroelastic control of turbomachines, Ph.D. thesis, Massachusetts Institute of Technology (2000).

[26] B. I. Epureanu, E. H. Dowell, K. C. Hall, Reduced-order models of unsteady transonic viscous flows in turbomachinery, Journal of Fluids and Structures 14 (8) (2000) 1215–1234.

[27] B. I. Epureanu, A parametric analysis of reduced order models of viscous flows in turbomachinery, Journal of fluids and structures 17 (7) (2003) 971–982.

[28] D. Bistrian, R. Susan-Resiga, Weighted proper orthogonal decomposition of the swirling flow exiting the hydraulic turbine runner, Applied Mathematical Modelling 40 (5) (2016) 4057–4078.

[29] K. E. Willcox, J. Peraire, J. White, An arnoldi approach for generation of reduced-order models for turbomachinery, Computers & fluids 31 (3) (2002) 369–389.

[30] E. Liberge, M. Benaouicha, A. Hamdouni, Low order dynamical system for fluid-rigid body interaction problem using pod method, The International Journal of Multiphysics 2 (1).

[31] E. Liberge, A. Hamdouni, Reduced order modelling method via proper orthogonal decomposition (pod) for flow around an oscillating cylinder, Journal of fluids and structures 26 (2) (2010) 292–311.

[32] L. Rao, Pod combined with fictitious domain method for solving shape optimization problem, Journal of Computational Information Systems 9 (18).

[33] G. Tissot, L. Cordier, B. R. Noack, Feedback stabilization of an oscillating vertical cylinder by pod reduced-order model, in: Journal of Physics: Conference Series, Vol. 574, IOP Publishing, 2015, pp. 012–137.

[34] N. Akkari, A. Hamdouni, E. Liberge, M. Jazar, On the sensitivity of the pod technique for a parameterized quasi-nonlinear parabolic equation, Advanced Modeling and Simulation in Engineering Sciences 1 (1) (2014) 14.

[35] Y. Jin, K. Lu, L. Hou, Y. Chen, An adaptive proper orthogonal decomposition method for model order reduction of multi-disc rotor system, Journal of Sound and Vibration 411 (2017) 210–231.

[36] D. Amsallem, C. Farhat, T. Lieu, High-order interpolation of reduced-order models for near real-time aeroelastic prediction, in: Paper IF-081, International Forum on Aeroelasticity and Structural Dynamics, Stockholm, Sweden, 2007.

[37] D. Amsallem, C. Farhat, Interpolation method for adapting reduced-order models and application to aeroelasticity, AIAA journal 46 (7) (2008) 1803–1813.

[38] R. Mosquera, A. Hamdouni, A. El Hamidi, C. Allery, Pod-basis interpolation via inverse distance weighting on grassmann manifolds, Manuscript submitted to AIMS' Journals.

[39] R. Glowinski, P. Le Tallec, Augmented Lagrangian and operator-splitting methods in nonlinear mechanics, SIAM, 1989.

[40] L. Sirovich, Turbulence and the dynamics of coherent structures part i: coherent structures, Quarterly of applied mathematics 45 (3) (1987) 561–571.

[41] Y.-C. Wong, Differential geometry of grassmann manifolds, Proceedings of the National Academy of Sciences 57 (3) (1967) 589–594.

[42] A. Logg, G. N. Wells, J. Hake, Dolfin: A c++/python finite element library, in: Automated Solution of Differential Equations by the Finite Element Method, Springer, 2012, pp. 173–225.

[43] D. N. Arnold, F. Brezzi, M. Fortin, A stable finite element for the stokes equations, CALCOLO 21 (4) (1984) 337–344.

[44] P. J. Holmes, J. L. Lumley, G. Berkooz, J. C. Mattingly, R. W. Wittenberg, Low-dimensional models of coherent structures in turbulence, Physics Reports 287 (4) (1997) 337–384.

[45] S. Volkwein, Proper orthogonal decomposition: Theory and reduced-order modelling, Lecture Notes, University of Konstanz 4 (2013) 4.

[46] L. Cordier, M. Bergmann, Proper orthogonal decomposition: an overview, Lecture series 2003-04 on post-processing of experimental and numerical data, Von Karman Institute for Fluid Dynamics. (2003) 46–pages.

[47] R. L. Burden, J. D. Faires, Numerical Analysis, 9th Edition, Richard Stratton, 2011.

Appendix A. Recalls on the POD

The Proper Orthogonal Decomposition (POD) has been introduced has a tools for the identification of coherent structures in dynamical systems in [19] based on previous works grounded in statistical analysis [20, 21, 22, 23]. Considering the spatial domain $\Omega \subset \mathbb{R}^d$ and the temporal domain $\mathrm{T} \subset \mathbb{R}$ with $\boldsymbol{x} \in \Omega$ and $t \in \mathrm{T}$. Then, the POD of a field $u : \Omega \times \mathrm{T} \to \mathbb{R}^d$ consists in finding a deterministic function $\boldsymbol{\phi}$ in a Hilbert space H which gives the optimum representation of u by solving the maximization problem

$$\frac{\left\langle (u|\,\phi)^2 \right\rangle}{(\phi|\,\phi)} = \max_{\psi \in H} \frac{\left\langle (u|\,\psi)^2 \right\rangle}{(\psi|\,\psi)} \tag{A.1}$$

where $\langle \bullet \rangle$ denotes a statistical average operator and $(\bullet|\,\bullet)$ denotes the inner product of H. We restrict ourselves to the application of POD to square integrable functions $H = L^2$. In this case, the maximization problem (A.1) is equivalent to the following eigenvalue problem:

$$\int_\Omega R(\boldsymbol{x}, \boldsymbol{x}')\, \phi(\boldsymbol{x}')\, \mathrm{d}\boldsymbol{x}' = \lambda\, \phi(\boldsymbol{x}) \tag{A.2}$$

where R is the non-negative symmetric spatial correlation tensor defined by

$$R(\boldsymbol{x}, \boldsymbol{x}') = \langle u(\boldsymbol{x}, t) \otimes u(\boldsymbol{x}', t) \rangle\,. \tag{A.3}$$

Moreover, if R is continuous, the following operator

$$\begin{array}{rccl} \mathcal{R}: & H & \to & H \\ & \phi(\bullet) & \mapsto & \int_\Omega R(\bullet, \boldsymbol{x}')\, \phi(\boldsymbol{x}')\, \mathrm{d}\boldsymbol{x}' \end{array} \tag{A.4}$$

is compact. Then, the Hilbert-Schmidt theorem ensures that there exists a set of positive eigenvalues $(\lambda_i)_{i\leq 1}$ decreasing toward zero:

$$\lambda_{i+1} > \lambda_i, \quad \lim_{i\to\infty} \lambda_i = 0 \tag{A.5}$$

and a set of eigenmodes $(\phi_i)_{1\leq i}$ which forms an orthonormal basis for H so that u can be decomposed as

$$u(\boldsymbol{x}, t) = \sum_{i=1}^{\infty} a_i(t)\, \phi_i(\boldsymbol{x}) \tag{A.6}$$

where the *POD temporal coefficient* are given by $a_i(t) = (u(\boldsymbol{x}, t)|\, \phi_i(\boldsymbol{x}))$ and the eigenmodes $(\phi_i)_{1\leq i}$ form the so called *POD basis* or Proper Orthogonal Modes (POMs). For details on the POD see [44, 45, 46]. In practice, the POMs can be obtained from a finite set of *snapshots* $\big(u(\boldsymbol{x}, t_n)\big)_{1\leq n\leq n_T}$ by the well known *snapshot POD* method introduced in [40] and recalled below.

1. Form the temporal correlation matrix $\mathbf{C}$ with elements:

$$[\mathbf{C}]_{mn} = (u(\boldsymbol{x}, t_m)|\, u(\boldsymbol{x}, t_n))\,. \tag{A.7}$$

2. Get the eigen decomposition of $\mathbf{C}$ such that

$$\mathbf{C} \cdot \boldsymbol{v}_i = \lambda_i \boldsymbol{v}_i. \tag{A.8}$$

3. Define the i-th POM as a linear combination of the snapshots from the coefficients of the i-th eigen-vector elements:

$$\phi_i(\boldsymbol{x}) = \sum_{j=1}^{n_T} [\boldsymbol{v}_i]_j\, u(\boldsymbol{x}, t_j). \tag{A.9}$$

Appendix B. Selection of the interpolation angles

In this appendix, we propose a greedy algorithm for the selection of the interpolation angles involved in the evaluation of the angular coefficient associated with the i-th POM of the characteristic function in section 3.3. We assume that the values for the i-th reference coefficient $(c_i^\star(\theta_n^\star))_{0\leq n\leq N^\star}$ defined in (23) are known for a set of $N^\star$ angles $\Theta^\star = [\theta_0^\star, \cdots, \theta_{N^\star}^\star]$ and that a procedure for the

construction of the periodic spline interpolant for the i-th coefficient S_i is available (see *e.g.* [47, §3.5]). Additionally, we define the relative spline interpolation error as

$$e_i(\theta) = \frac{|c_i^\star(\theta) - S_i(\theta)|}{c_i^{\mathrm{RMS}}}, \tag{B.1}$$

where c_i^{RMS} denotes the root-mean-square value:

$$c_i^{\mathrm{RMS}} = \sqrt{\frac{1}{N^\star} \sum_{n=0}^{N^\star} \left(c_i^\star(\theta_n^\star)\right)^2}. \tag{B.2}$$

The greedy selection is given in algorithm 3.

Data: Original set of angles $\Theta^\star = \left(\theta_n^\star\right)_{1 \le n \le N^\star}$.

Result: Reduced data set $\widehat{\Theta} = \left(\theta_n\right)_{1 \le n \le N_i}$.

Initialize $\widehat{\Theta} \leftarrow \left(\theta_0^\star, \theta_{N^\star}^\star\right)$ and $N_i \leftarrow 1$;

while $\max\limits_{\theta^\star \in \Theta^\star} e_i(\theta^\star) > \varepsilon_\theta$ **do**

  Find j *s.t.* $e_i(\theta_j^\star) = \max\limits_{\theta^\star \in \Theta^\star} e_i(\theta^\star)$;

  Insert $\theta_j^\star$ in $\widehat{\Theta}$;

  Increment $N_i \leftarrow N_i + 1$;

end

Algorithm 3: Greedy algorithm to select the set of angles for the construction of the periodic spline interpolant for the evaluation of the angular coefficients associated with the characteristic function in (18).

Appendix C. Additional results

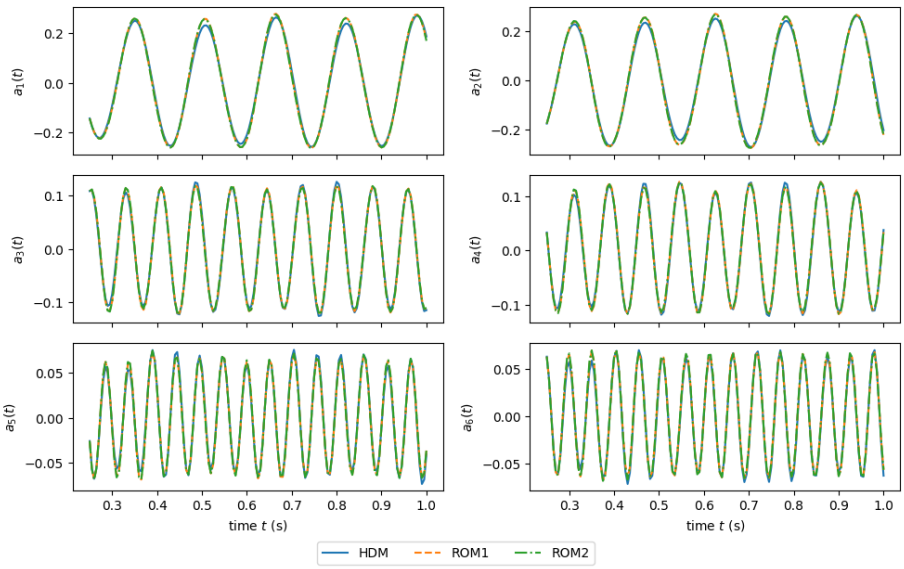

Figure C.12: Temporal evolution of the coefficients for the fluctuating part of the velocity in the steady case (see 5.2.1). The coefficients for the HDM are obtained by projection of the snapshots over the POD modes $a_i(t) = \left(\boldsymbol{u}_h(\boldsymbol{x}, t) | \, \boldsymbol{\phi}_i^{\boldsymbol{u}}(\boldsymbol{x})\right)$. The coefficients for the ROM1 and the ROM2 are obtained from the solution of (15) and (21), respectively.

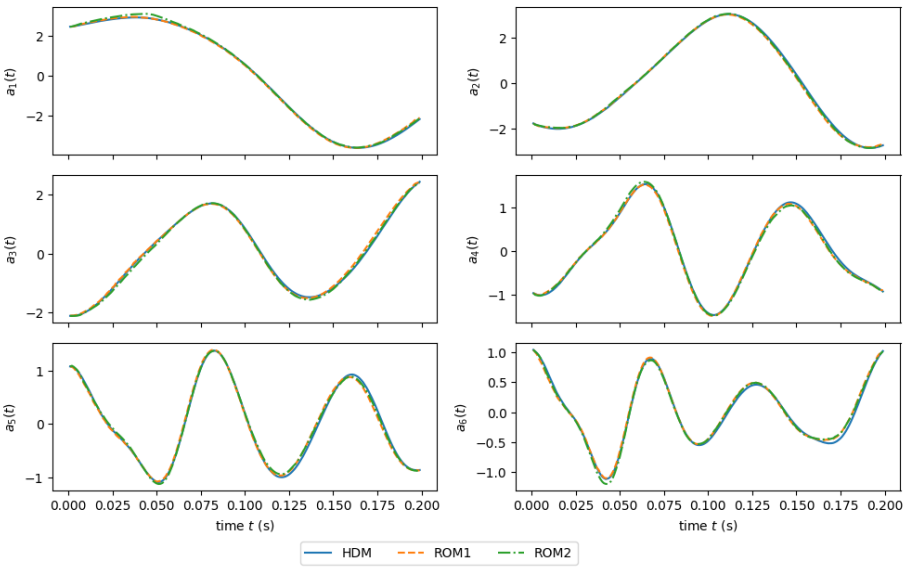

Figure C.13: Temporal evolution of the coefficients for the fluctuating part of the velocity during the transient period (see 5.2.2). The coefficients for the HDM are obtained by projection of the snapshots over the POD modes $a_i(t) = \left(\boldsymbol{u}_h(\boldsymbol{x},t) | \, \boldsymbol{\phi}_i^{\boldsymbol{u}}(\boldsymbol{x})\right)$. The coefficients for the ROM1 and the ROM2 are obtained from the solution of (15) and (21), respectively.

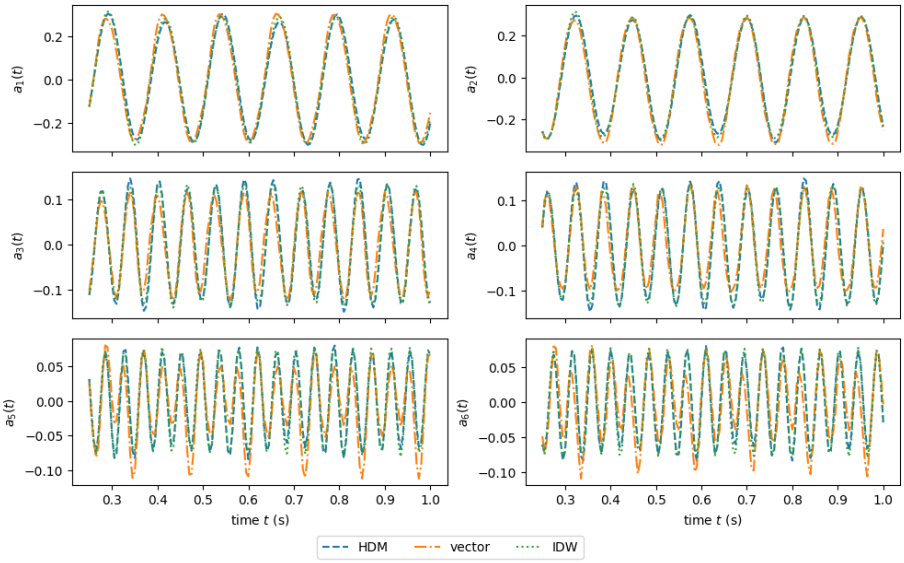

Figure C.14: Temporal evolution of the coefficients for the fluctuating part of the velocity in the interpolation case (see section 5.3). The coefficients for the HDM are obtained by projection of the snapshots over the POD modes $a_i(t) = \left(\boldsymbol{u}_h(\boldsymbol{x},t)|\,\boldsymbol{\phi}_i^{\boldsymbol{u}}(\boldsymbol{x})\right)$. The coefficients labeled vec and idw are obtained from the solution of (21) for the ROM2 constructed from the bases interpolated by a naive method and by the method described in section 4, respectively.